

# 1 Nonlinear increase in seawater $^{87}\text{Sr}/^{86}\text{Sr}$ in the Oligocene to 2 early Miocene and implications for climate-sensitive 3 weathering

4  
5 Heather M. Stoll<sup>1</sup>, Leopoldo D. Pena<sup>2</sup>, Ivan Hernandez-Almeida<sup>1</sup>, Jose Guitian<sup>1\*</sup>, Thomas  
6 Tanner<sup>1</sup>, Heiko Pälike<sup>3</sup>

7 <sup>1</sup>Department of Earth Science, ETH Zurich, Zurich, 8092 Switzerland

8 <sup>2</sup>GRC Geociències Marines, Dept. Dinàmica de la Terra i de l'Oceà, Facultat de Ciències de la Terra, Universitat  
9 de Barcelona, Barcelona, 28080 Spain

10 <sup>3</sup>MARUM Centre for Marine Environmental Sciences, University of Bremen, Bremen, 28359 Germany

11  
12 *Correspondence to:* Heather M. Stoll ([heather.stoll@erdw.ethz.ch](mailto:heather.stoll@erdw.ethz.ch))

13 *\*Present address:* Centro de Investigación Mariña, Universidade de Vigo, GEOMA, Vigo, 36310, Spain

14 **Abstract.** The  $^{87}\text{Sr}/^{86}\text{Sr}$  of marine carbonates provides a key constraint on the balance of continental weathering  
15 and hydrothermal Sr fluxes to the ocean, and mid-Oligocene to mid-Miocene features the most rapid rates of  
16 increase in the  $^{87}\text{Sr}/^{86}\text{Sr}$  of the Cenozoic. Because previous records of the  $^{87}\text{Sr}/^{86}\text{Sr}$  increase with time were based  
17 on biostratigraphically defined age models in diverse locations, it was difficult to unambiguously distinguish m.y.  
18 scale variations in the rate of  $^{87}\text{Sr}/^{86}\text{Sr}$  change from variations in sedimentation rate. In this study, we produce  
19 the first  $^{87}\text{Sr}/^{86}\text{Sr}$  results from an Oligocene to early Miocene site with a precise age model derived orbital tuning  
20 of high resolution benthic  $\delta^{18}\text{O}$ , at the Equatorial Pacific Ocean Drilling Program (ODP) Site 1218. Our new  
21 dataset resolves transient decreases in  $^{87}\text{Sr}/^{86}\text{Sr}$ , as well as periods of relative stasis. These changes can be directly  
22 compared with the high resolution benthic  $\delta^{18}\text{O}$  in the same site. We find slowing of the rate of  $^{87}\text{Sr}/^{86}\text{Sr}$  increase  
23 coincides with the onset of Antarctic ice expansion at the beginning of the Mid-Oligocene Glacial Interval, and a  
24 rapid steepening in the  $^{87}\text{Sr}/^{86}\text{Sr}$  increase coincides with the benthic  $\delta^{18}\text{O}$  evidence for rapid ice retreat. This pattern  
25 may reflect either northward shifts in the Intertropical Convergence Zone precipitation to areas of nonradiogenic  
26 bedrock, and/or lowered weathering fluxes from highly radiogenic glacial flours on Antarctic. We additionally  
27 generate the first  $^{87}\text{Sr}/^{86}\text{Sr}$  data from ODP Site 1168 on the Tasman Rise and Integrated Ocean Drilling Program  
28 (IODP) Site 1406 of the Newfoundland Margin during the Oligocene to early Miocene to improve the precision  
29 of age correlation of these Northern Hemisphere and Southern Hemisphere mid-latitude sites, and to better  
30 estimate the duration of early Miocene hiatus and condensed sedimentation.

## 31 32 **1 Introduction**

33 The mid-Oligocene through the mid-Miocene features the fastest rate of change in seawater  $^{87}\text{Sr}/^{86}\text{Sr}$  of  
34 the Cenozoic, evidence of significant change in the balance of Sr sources to the ocean. Although the precise

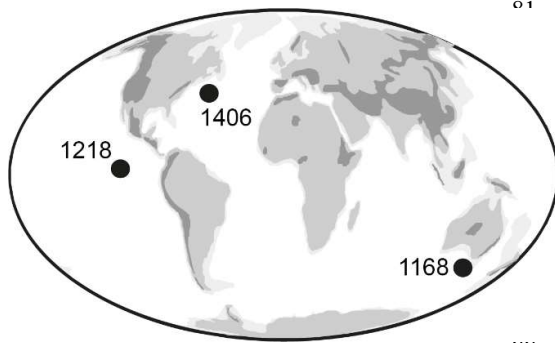
35 causes of the Cenozoic  $^{87}\text{Sr}/^{86}\text{Sr}$  change remain under discussion, to first order the rise reflects an increase in the  
36 supply of dissolved Sr sourced from weathering of older rocks of higher  $^{87}\text{Sr}/^{86}\text{Sr}$ , which are found on continents,  
37 compared to the supply of dissolved Sr from rocks of lower  $^{87}\text{Sr}/^{86}\text{Sr}$  characterizing submarine volcanic  
38 weathering and subaerial weathering of young volcanic provinces (Palmer and Elderfield, 1985). This change in  
39 balance of sources can be accomplished by one or more processes including decrease in rate of hydrothermal  
40 weathering, increase in total continental weathering, or changes in the  $^{87}\text{Sr}/^{86}\text{Sr}$  of continental weathering flux due  
41 to either changes in the location of most intense weathering or changes in the composition and average age  
42 (Peucker-Ehrenbrink and Fiske, 2019) of rocks exposed to weathering.

43 The Oligocene-early Miocene is a period of very rapid increase in  $^{87}\text{Sr}/^{86}\text{Sr}$ , with multiple possible drivers  
44 including the unroofing of highly radiogenic source rocks in the Himalaya (Galy et al., 1996; Yang et al., 2022;  
45 Myrow et al., 2015). Within the Oligocene-early Miocene period of rapid increase in  $^{87}\text{Sr}/^{86}\text{Sr}$ , some previous  
46 studies have suggested the potential for 1-3 million year timescale variations in the rate of increase (Oslick et al.,  
47 1994) and proposed that the liberation of Sr from silicate weathering may respond to changes in the production  
48 and exposure of glacially floured rock on Antarctica (Miller et al., 1991; Oslick et al., 1994; Zachos et al., 1999).  
49 However, the precision of estimates of the rate of change in  $^{87}\text{Sr}/^{86}\text{Sr}$  are limited by the precision of the  
50 independent age model in marine records. Where age model control points are of low resolution or low certainty,  
51 changes in sedimentation rate may cause apparent variations in the rate of change in  $^{87}\text{Sr}/^{86}\text{Sr}$ , so that changes in  
52 the rate of  $^{87}\text{Sr}/^{86}\text{Sr}$  cannot be confidently inferred. To date, available  $^{87}\text{Sr}/^{86}\text{Sr}$  data for the Oligocene and early  
53 Miocene is derived from deep sea sediment cores featuring only biostratigraphically derived age models, whose  
54 precision is limited by the biostratigraphic sampling resolution as well as the potential for diachroneity among  
55 events. Precision on such age models can be limited by long distances between examined biostratigraphic points  
56 in the core and the potential for diachroneity in the first occurrence or last occurrence of taxa in diverse locations,  
57 and may feature uncertainties from 0.5 to 4 million years (Miller et al., 1988). Over the last decade,  
58 astrochronology has emerged as a powerful independent chronometer, and the success of continuous coring and  
59 splicing of deep ocean sediment cores has enabled the elaboration of precise independent age models based on  
60 orbital tuning of high resolution benthic  $\delta^{18}\text{O}$  records (Pälike et al., 2006; Liebrand et al., 2016; Westerhold et al.,  
61 2020; De Vleeschouwer et al., 2017).

62 In this study, we seek to apply the independent orbitally tuned Oligocene chronology for two purposes.  
63 First, we seek to evaluate the potential for dynamic changes in Sr sources by producing a  $^{87}\text{Sr}/^{86}\text{Sr}$  record from a  
64 site with an independent orbitally-resolved age model, Ocean Drilling Program (ODP) Site 1218 from the  
65 Equatorial Pacific (Figure 1), for which original chronology (Pälike et al., 2006) was recently updated (Westerhold  
66 et al., 2020). The very rapid rate of change in seawater  $^{87}\text{Sr}/^{86}\text{Sr}$  also provides the opportunity for improved age  
67 correlation among distal sites (Mcarthur et al., 2020). Therefore, our second objective is to improve the fidelity  
68 of the age model for two further sites which currently lack an orbitally resolved age model, using existing reference  
69 curves and the Site 1218 record as an additional reference. For this objective, we focus on North Atlantic  
70 International Ocean Discovery Program Site 1406 (Newfoundland Margin) and Southern Ocean ODP Site 1168  
71 (Tasman Rise), both emerging as important sites for Oligocene to early Miocene paleoceanographic studies (Scher  
72 et al., 2015; Hoem et al., 2022; Hoem et al., 2021; Guitián and Stoll, 2021; Kim and Zhang, 2022; Egger et al.,  
73 2018; Liu et al., 2018; Spray et al., 2019; Boyle et al., 2017). At site 1406, Sr isotope stratigraphy improves  
74 constraints on the duration of an early Miocene hiatus (van Peer et al., 2017b; Norris et al., 2014). The Oligocene

75 to Early Miocene Southern Ocean paleogeography produced strong provincialism in many marine taxa from Site  
76 1168, so synchronicity with global biostratigraphic datums is uncertain. For paleoclimatic study, tuning to Site  
77 1218 offers the advantage of providing a precise link with the complete benthic  $\delta^{18}\text{O}$  record and therefore enabling  
78 direct correlation to the highest resolution paleoclimatic record available for this time interval.

79 **Figure 1. Location of ODP 1218, IODP 1406, and ODP 1168 with paleogeography during the Oligocene-Miocene**  
80 **Transition. Reconstruction was made using the plate tectonic reconstruction service ODSN ([www.odsn.de](http://www.odsn.de)).**



## 2 Sites and Methods

### 2.1 Sediments

Ocean Drilling Program (ODP) Leg 199, Site  
Site 1218, equatorial Pacific ( $8^{\circ}53.378'\text{N}$ ,  $135^{\circ}22.00'\text{W}$ ,  
4.8-km water depth) features a detailed astrochronologic  
age model from benthic  $\delta^{18}\text{O}$  originally spanning 22 to  
25 Ma (Pälike et al., 2006). Subsequently, continuous  
tuning at precision of the 100 ky eccentricity cycle from

89 21.81 Ma through the lowermost Oligocene was generated on the CENOGRID timescale (Westerhold et al.,  
90 2020). In Site 1218 we sought high resolution in the Middle Oligocene Glacial Interval (MOGI), previously  
91 hypothesized to feature inflection points in the  $^{87}\text{Sr}/^{86}\text{Sr}$  curve (Oslick et al., 1994). We targeted samples between  
92 59.93 and 211.94 revised meter core depth (rmcd). Due to the modest carbonate content of Site 1218, not all  
93 targeted sample intervals contained sufficient foraminifera for analysis. We have picked  $>2$  mg of mixed species  
94 of planktonic or mixed species of benthic foraminifera, depending on the abundance in each sample. From some  
95 samples, populations of both benthic and planktic forams could be procured and we report the averaged  $^{87}\text{Sr}/^{86}\text{Sr}$   
96 ratio for the two populations.

97

98 Integrated Ocean Drilling Program (IODP) Expedition 342 recovered Paleogene to Neogene sedimentary  
99 sequences in contourite drift deposits off the coast of Newfoundland in the Northwestern Atlantic. Here we focus  
100 on Site 1406 ( $40^{\circ}21.0'\text{N}$ ,  $51^{\circ}39.0'\text{W}$ ; 3814 mbsl) with samples dominantly from Hole A, but including a few  
101 samples from Holes B and C. The composite depth scale for the site (CCSF-A) is based on physical properties  
102 and trace element ratios from XRF Scanner (van Peer et al., 2017b) and is under revision as further benthic  
103 foraminifera and fine fraction stable isotope data are produced. Consequently, where samples from all sites are  
104 plotted, we illustrate on the composite CCSF-A scale but where exclusively data from Hole A are presented, we  
105 illustrate depth on CSF-A scale as this latter scale will not be revised; both depth scales are provided in data tables.  
106 Based on available biostratigraphy and previous age models (Norris et al., 2014) (van Peer et al., 2017b), we  
107 sought samples spanning age range 17 to 30 Ma, represented by depths from 23.9 to 200 m on the CCSF-A depth  
108 scale. In the Southern Hemisphere, ODP Site 1168 was drilled offshore of the Australian plate at the western  
109 margin of Tasmania, at  $43^{\circ}36.57'\text{S}$  and  $139^{\circ}144'24.76'\text{E}$ , and 2463m water depth. This sequence is within a  
110 graben-developed basin with sediment accumulation since the latest Eocene (Exon et al., 2004). Based on  
111 available biostratigraphy (Stickley et al., 2004), we selected samples from Hole A, spanning the 16 to 27 Ma  
112 interval, representing sediments from 278 to 562 m depth on the mbsf depth scale used for ODP sites of this  
113 generation. Mixed planktonic foraminifera were picked for both sites 1406 and 1168.

114 **2.2 Analytical**

115 Strontium isotope ratios ( $^{87}\text{Sr}/^{86}\text{Sr}$ ) were measured on ~2 mg of cleaned foraminifera carbonates.  
116 Foraminifera samples were crushed open under binocular inspection and the fragments were rinsed several times  
117 in MilliQ water, methanol and ultrasonicated to remove detrital contaminants (Pena et al., 2005). Each sample  
118 was treated individually to ensure that sufficient rinsing steps were applied. Cleaned fragments were dissolved in  
119 dilute double distilled nitric acid, and the resulting solution centrifuged at medium speed for 20 minutes to remove  
120 any potential detrital material left in the samples. The supernatant was transferred to clean Savillex-PFA beakers  
121 and Sr was chemically separated from sample matrix and interfering Rb using Triskem Sr-Spec resin through  
122 column chromatography procedures at the LIRA ultra-clean laboratory (Universitat de Barcelona).

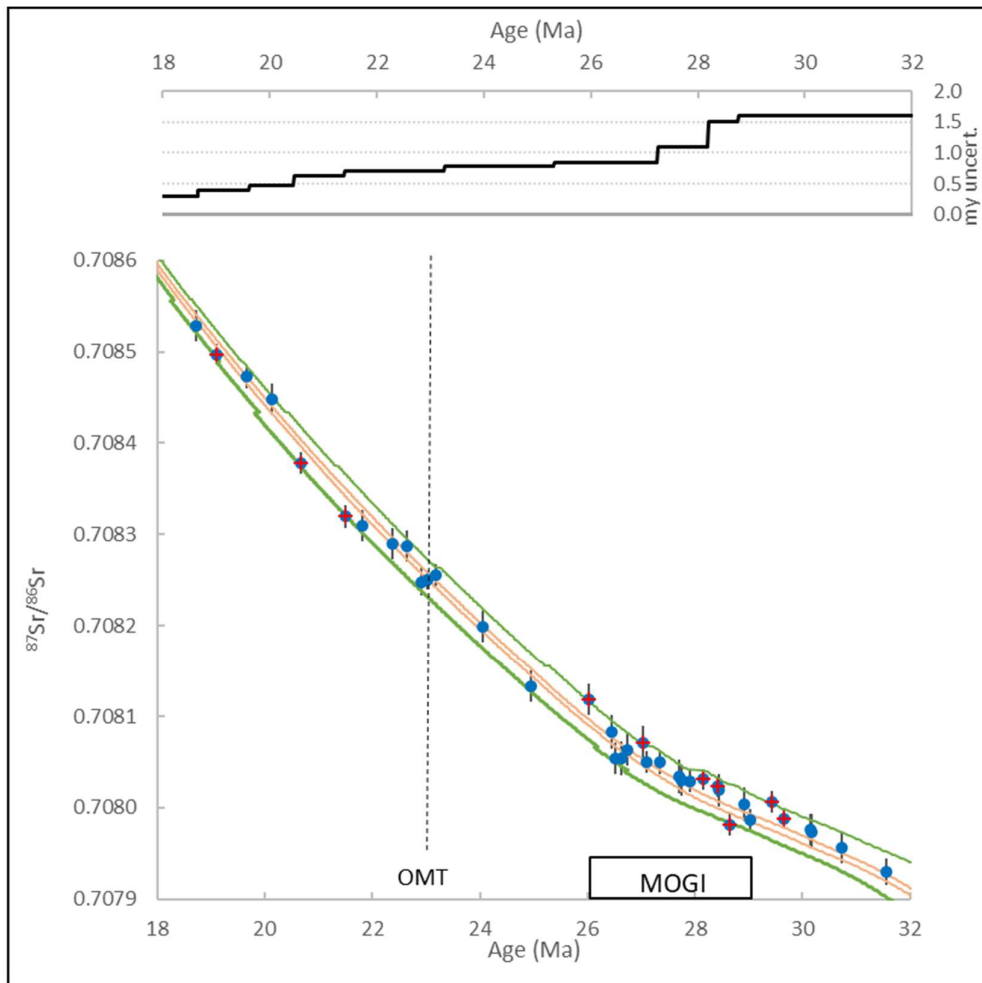
123 Following sample purification, Sr isotope ratios were determined by multicollector inductively coupled  
124 mass spectrometry on a Nu Instruments (Wrexham, UK) Plasma 3 MC-ICPMS at the University of Barcelona  
125 (CciT-UB). For the determination of the  $^{87}\text{Sr}/^{86}\text{Sr}$  isotope ratios, the contribution of  $^{87}\text{Rb}$  to the  $^{87}\text{Sr}$  signal was  
126 corrected from the measurement of the  $^{85}\text{Rb}$  signal, assuming a  $^{87}\text{Sr}/^{85}\text{Sr}$  ratio of 0.38562. The  $^{86}\text{Kr}$  interference  
127 on  $^{86}\text{Sr}$ , caused by impurities in the argon gas, was also corrected by measuring the  $^{83}\text{Kr}$  signal, and assuming a  
128  $^{83}\text{Kr}/^{86}\text{Kr}$  value of 0.66453.  $^{87}\text{Sr}/^{86}\text{Sr}$  ratios were normalized for instrumental mass bias to  $^{86}\text{Sr}/^{88}\text{Sr} = 0.1194$ .  
129 Instrumental drift was corrected by sample-standard bracketing (SSB) using NBS987 = 0.710249 as the primary  
130 standard with matching standard and sample Sr concentrations. External analytical reproducibility during the  
131 session was  $\pm 0.000018$  ( $2\sigma$ ,  $n=19$ ). Procedural blanks are routinely measured at every analytical session. Typical  
132 procedural Sr blanks (including sample cleaning, purification and analysis) are  $369 \pm 264$  pg,  $n=12$ ,  $1\sigma$ . Blanks  
133 are systematically corrected for every measurement and the effect of the correction is in the sixth decimal place  
134 of the  $^{87}\text{Sr}/^{86}\text{Sr}$  ratios, well below the external reproducibility of the analytical method (5th decimal place). Values  
135 are normalized to SRM 987 using  $^{86}\text{Sr}/^{86}\text{Sr}$  of 0.1194 and  $^{87}\text{Sr}/^{86}\text{Sr}$  of 0.710249. This is identical to the  
136 normalization of (Mcarthur et al., 2020) using  $^{87}\text{Sr}/^{86}\text{Sr}$  0.709174 for modern marine-Sr (EN-1 and similar),  
137 equivalent to 0.710248 for SRM(NIST) 987.

138 **3 Results**

139 Our new data from Site 1218 on the Cenogrid age model (Figure 2, Table 1), reveal a similar long term  
140 amplitude and rate of rise in  $^{87}\text{Sr}/^{86}\text{Sr}$  as previously reported data on biostratigraphically constrained age models  
141 (Mcarthur et al., 2020). However, the new data reveal a 1 m.y. duration period of negligible  $^{87}\text{Sr}/^{86}\text{Sr}$  rise (27-28  
142 Ma) and local reversals in the overall trend of increasing  $^{87}\text{Sr}/^{86}\text{Sr}$  during the Middle Oligocene Glacial Interval  
143 (MOGI) and at the Oligo-Miocene transition. The new data also reveal several intervals of especially abrupt  
144 increase in  $^{87}\text{Sr}/^{86}\text{Sr}$  within and at the end of the MOGI.

145

146



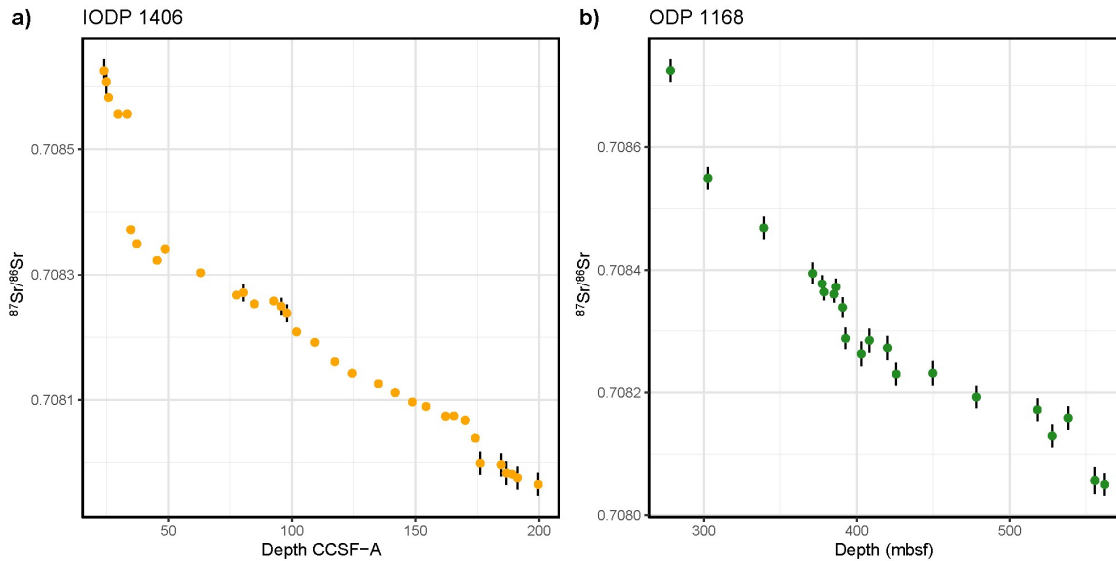
147

148 **Figure 2:**  $^{87}\text{Sr}/^{86}\text{Sr}$  results from Site 1218 (blue circles with  $2\sigma$  analytical uncertainty shown). The orange lines show  
 149 the upper and lower bounds of the LOESS fit of biostratigraphically defined  $^{87}\text{Sr}/^{86}\text{Sr}$  (Mearthur et al., 2020). Samples  
 150 falling outside the biostratigraphically defined long term curve are highlighted in red. The green lines illustrate  
 151 expanded age bounds for LOESS fit of biostratigraphically constrained age models (Mearthur et al., 2020). Upper  
 152 panel illustrates the width of the age uncertainty of the expanded bounds. The Middle Oligocene Glacial Interval  
 153 (MOGI) from 29 to 26 Ma is labelled, as is the Oligocene-Miocene Transition (OMT). We highlight this duration of  
 154 MOGI on the basis of the 1218 benthic  $\delta^{18}\text{O}$  record as indicated in Figure 4; it is slightly longer than the 28 to 26.3 Ma  
 155 MOGI defined by (Liebrand et al., 2016; Liebrand et al., 2017)

156

157 In Site U1406, a prominent reversal in the  $^{87}\text{Sr}/^{86}\text{Sr}$  rise is observed between 48.7 and 45.4 m (Figure 3a,  
 158 depths described on the CCSF-A scale). A significant jump in  $^{87}\text{Sr}/^{86}\text{Sr}$  suggests an appreciable hiatus between  
 159 33.3 m and 34.7 m. The abrupt change in  $^{87}\text{Sr}/^{86}\text{Sr}$  between 176.2 and 170.1 may also indicate a hiatus or  
 160 significantly condensed interval. In Site 1168 (Figure 3b), a prominent reversal in the  $^{87}\text{Sr}/^{86}\text{Sr}$  rise occurs between  
 161 538.2 and 527.8 m CSF-A.

162



163

164 **Figure 3:**  $^{87}\text{Sr}/^{86}\text{Sr}$  results from a) U1406 and b) 1168. Vertical error bars indicate  $2\sigma$  analytical uncertainty where it  
 165 exceeds the size of the plotted symbol.

166 **4 Discussion**

167 **4.1 Variation in the rate of change of  $^{87}\text{Sr}/^{86}\text{Sr}$  in Site 1218**

168

169 The steep long term Oligocene to early Miocene increase in  $^{87}\text{Sr}/^{86}\text{Sr}$  is long recognized and variably  
 170 attributed to exhumation of readily weathered radiogenic bedrock during the Himalayan orogeny (Krishnaswami  
 171 et al., 1992; Raymo et al., 1988), or to accelerated weathering of radiogenic bedrock in Antarctica with the onset  
 172 of its glaciation (Miller et al., 1991). The cause of this long term increase is beyond the scope of this study and  
 173 our focus is on the variability in the rate of increase within the Oligocene to early Miocene.

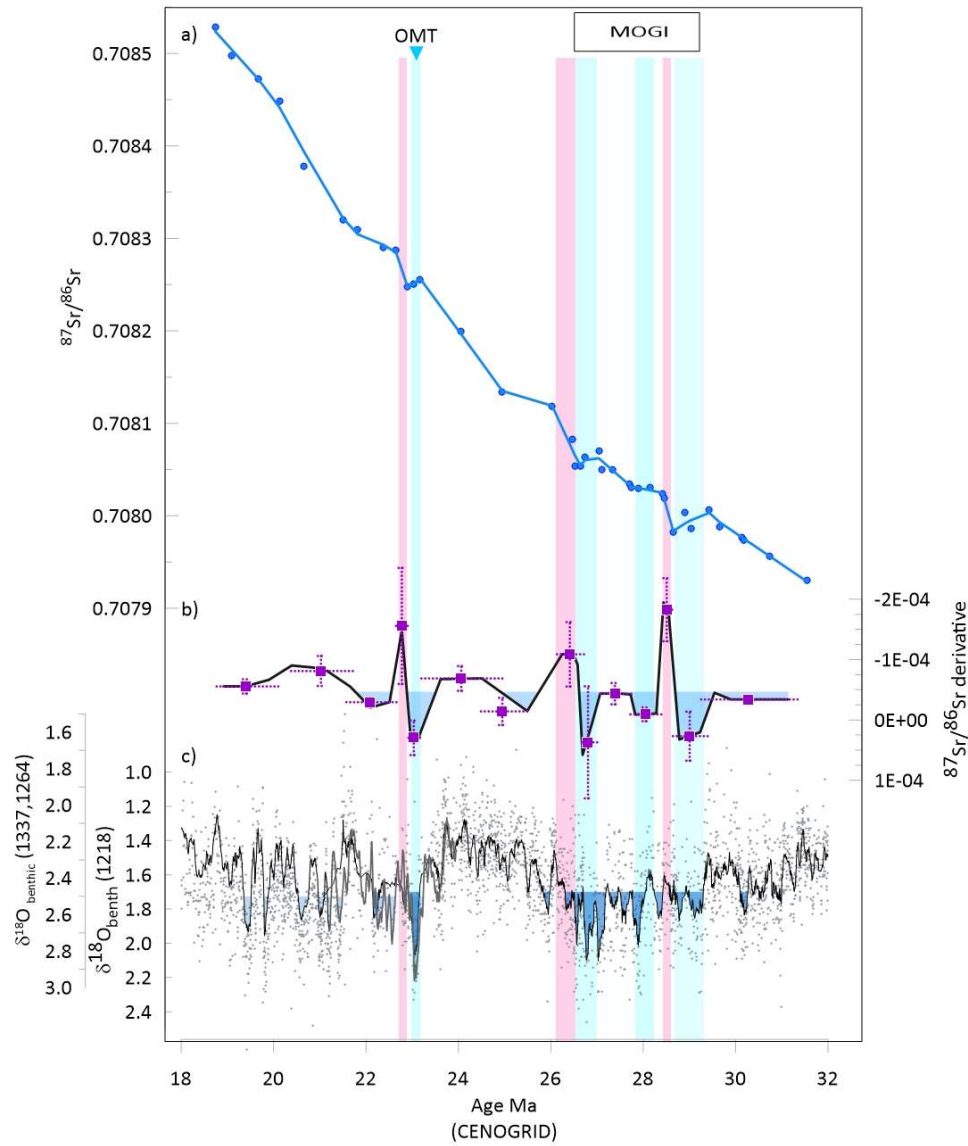
174 Significantly, the precise independent chronology of Site 1218 confirms that the long term Oligocene  
 175 and early Miocene increase in  $^{87}\text{Sr}/^{86}\text{Sr}$  is punctuated by significant structure, including reversals, periods of  
 176 negligible  $^{87}\text{Sr}/^{86}\text{Sr}$  increase, as well as more abrupt increases in  $^{87}\text{Sr}/^{86}\text{Sr}$ . Reversals beyond analytical  
 177 uncertainty are also seen in published high resolution Mid-Oligocene  $^{87}\text{Sr}/^{86}\text{Sr}$  records from both ODP Site 522  
 178 (Reilly et al., 2002) and ODP Site 689B (Mead and Hodell, 1995), suggesting that they are a robust feature of the  
 179 Oligocene ocean Sr cycle. The uncertainty in absolute chronology complicates the inference of m.y. scale periods  
 180 of stasis or abrupt  $^{87}\text{Sr}/^{86}\text{Sr}$  increase in previously published records with biostratigraphic age models. To further  
 181 evaluate how the rate of change of  $^{87}\text{Sr}/^{86}\text{Sr}$  deviates from a monotonic increase from 32 to 18 Ma, we generate  
 182 a smoothed fit to the data based on local linear regression model (Figure 4). In the model, local regressions were  
 183 based on 3 to 6 consecutive samples and age range of at least 0.25 Ma, with the exception of a single shorter span  
 184 of only 0.18 Ma at 26 Ma. To estimate the rate of change, we illustrate the derivative of this smoothed fit, as well  
 185 as the slope and its uncertainty for each linear segment (Figure 4b). This analysis illustrates periods of both more  
 186 rapid increase as well as slowed  $^{87}\text{Sr}/^{86}\text{Sr}$  increase or a decrease.

187 In Site 1218, appreciably lower rates of  $^{87}\text{Sr}/^{86}\text{Sr}$  increase (or even  $^{87}\text{Sr}/^{86}\text{Sr}$  decrease) occur centered at  
 188 29 Ma and 26.8 Ma during the MOGI, and at 23 Ma during the OMT (Figure 4). Each of these periods is followed

189 by a large acceleration of  $^{87}\text{Sr}/^{86}\text{Sr}$  increase. Our new data provide the most precise comparison between  $^{87}\text{Sr}/^{86}\text{Sr}$   
190 and the benthic  $\delta^{18}\text{O}$  record of deep sea temperature and ice volume because the records derive from the same  
191 deep sea sediment archive (without correlation uncertainty) and the benthic  $\delta^{18}\text{O}$  record is very high resolution,  
192 without aliasing which can occur in records sampled at resolution comparable or greater than periods of orbital  
193 variation. The earliest slowing in the rate of  $^{87}\text{Sr}/^{86}\text{Sr}$  increase and even decrease in  $^{87}\text{Sr}/^{86}\text{Sr}$  which we resolve  
194 (centered at 29 Ma) coincides with the onset of heavier average benthic  $\delta^{18}\text{O}$  demarcating the Mid-Oligocene  
195 Glacial interval (MOGI), and the recovery of rapid  $^{87}\text{Sr}/^{86}\text{Sr}$  increase coincides with a shift towards more negative  
196 benthic  $\delta^{18}\text{O}$  (ice volume decrease and/ or deep sea warming). The return to more intense glaciation from 28 to  
197 26.8 Ma yields a decrease in  $^{87}\text{Sr}/^{86}\text{Sr}$ . The subsequent acceleration of  $^{87}\text{Sr}/^{86}\text{Sr}$  increase at 26.5 Ma coincides  
198 with the onset of the negative shift in benthic  $\delta^{18}\text{O}$  marking the end of the MOGI with ice volume decrease and/  
199 or deep sea warming. The reduction of  $^{87}\text{Sr}/^{86}\text{Sr}$  increase (or  $^{87}\text{Sr}/^{86}\text{Sr}$  decrease) at the OMT coincides with an  
200 intense glacial phase, and subsequently a consequent acceleration of  $^{87}\text{Sr}/^{86}\text{Sr}$  increase at the end of the glacial  
201 phase. This event may coincide with the post-OMT acceleration previously defined as 22.4 Ma on the Cande and  
202 Kent (Cande and Kent, 1992) timescale (Oslick et al., 1994). We are unable to evaluate if there are similar <0.5  
203 Ma variations in the rate of  $^{87}\text{Sr}/^{86}\text{Sr}$  change between 26 and 23 Ma as our sample resolution is not high enough  
204 in this interval. The main changes in slope are significant at the 68% CI (1s) level, but an increase in the sample  
205 resolution and number of data points would be needed to confidently distinguish many of these differences at the  
206 95% CI (2s) level.

207 Variations in the isotopic composition of Sr inputs on timescales of  $10^5$  yr are not expected to reflect  
208 changes in ocean crustal production rate and hydrothermal flux, nor significant changes in the composition of  
209 bedrock exposed on continents. Therefore, such changes are suggestive of change in either the intensity of  
210 continental weathering relative to hydrothermal sources or changes in the locus of most intense continental  
211 weathering among continental sources of contrasting  $^{87}\text{Sr}/^{86}\text{Sr}$ . For example, a short term relative increase in  
212 weathering intensity in areas underlain by younger average bedrock compared to older average bedrock would  
213 lead to a decreased  $^{87}\text{Sr}/^{86}\text{Sr}$  of the riverine Sr flux and the marine reservoir. Alternatively, a short term decrease  
214 in the intensity of weathering and thereby in the continental Sr flux (higher  $^{87}\text{Sr}/^{86}\text{Sr}$  than the hydrothermal flux)  
215 could also lead to a decreased marine  $^{87}\text{Sr}/^{86}\text{Sr}$ . In either case, the long residence time of Sr in the ocean would  
216 result in lags between onset of elevated fluxes and peak response in ocean chemistry and would cause significant  
217 attenuation of the time-varying input signal. An example of the phasing and amplitude variation in the  $^{87}\text{Sr}/^{86}\text{Sr}$   
218 of the Sr influx which could yield the observed trends in marine  $^{87}\text{Sr}/^{86}\text{Sr}$  is illustrated in Supplementary Figure  
219 1. for a sample residence time of 2.5 million years as suggested by (Hodell et al., 1990) Hodell et al., 1990. A  
220 shorter residence time has been proposed for the Oligocene by (Paytan et al., 2021); for a shorter residence time,  
221 a less extreme forcing would be required to simulate our observations. We caution that because the Sr isotopic  
222 system of the Oligocene to Early Miocene is underconstrained, the observations of oceanic  $^{87}\text{Sr}/^{86}\text{Sr}$  do not provide  
223 a unique solution for the variation in fluxes and/or their isotopic composition.

224



225

226 **Figure 4. a)** Measured Site 1218  $^{87}\text{Sr}/^{86}\text{Sr}$  (symbols) and the smoothed fit from local linear regression (blue line). **b)** the  
 227 derivative of the smoothed fit (black line) and the slope of each linear segment (purple square), together with the  
 228 uncertainty on the slope (vertical error bar, 68% confidence interval) and the age range of the local linear fit (horizontal bar).  
 229 Shading indicates sectors in which  $^{87}\text{Sr}/^{86}\text{Sr}$  rises more slowly than the average rate over 32 to 18 Ma. **c)** Benthic  $\delta^{18}\text{O}$   
 230 measurements (gray points) and lines showing 20 point running mean. From Site 1218 (black line from 21.46 to 32 Ma)  
 231 (Pälike et al., 2006) and from the Cenozoic reference splice derived from U1337 (Holbourn et al., 2015) and ODP Site  
 232 1264 (Westerhold et al., 2020) both scaled as in (Westerhold et al., 2020), as gray line from 21.2 to 24 Ma when  
 233 overlapping with 1219 record, and black line from 18 to 21.2 Ma. All data are plotted on the orbitally tuned  
 234 CENOGRID timescale (Westerhold et al., 2020). Blue shading highlights intervals with benthic  $\delta^{18}\text{O}$  more positive  
 235 than 1.7 ‰ in Site 1218 and 2.5 ‰ in Cenozoic reference splice 1264 and U1337. The Middle Oligocene Glacial Interval  
 236 (MOGI) from 29 to 26 Ma is labelled, as is the Oligocene-Miocene Transition (OMT). Vertical blue and pink lines  
 237 highlight intervals of slower and more rapid rate of change in  $^{87}\text{Sr}/^{86}\text{Sr}$ , respectively.

238

239 The coincidence of periods of slowed  $^{87}\text{Sr}/^{86}\text{Sr}$  and the onset of glacial advance on Antarctica evidenced  
 240 in benthic  $\delta^{18}\text{O}$  suggests a climate control on the variations in the continental Sr flux on  $10^5$  yr timescales from  
 241 one or both of these mechanisms. Changes in the location of intense rainfall, such as shift in the polar front or  
 242 Intertropical Convergence Zone (ITCZ), could alter the locus of most intense weathering. Potentially, episodes  
 243 of Antarctic glacial expansion could cause an equatorward movement of the SH westerlies and associated rainfall  
 band, or could cause a mean ITCZ shift toward the northern Hemisphere. However, climatically-driven changes



244 in the position of main heavy rainfall belts such as ITCZ is usually limited to < 10 degrees latitude and may be  
245 longitudinally variable (Atwood et al., 2020). A movement of precipitation belts would have a significant  
246 consequence on global riverine  $^{87}\text{Sr}/^{86}\text{Sr}$  only in cases of fortuitous distribution of bedrock of widely different  
247 ages across the length scale of ITCZ movement. If a northward shift of the mean ITCZ significantly increased  
248 the Sr flux from a region of nonradiogenic Sr, the marine  $^{87}\text{Sr}/^{86}\text{Sr}$  could experience a transient decrease. One  
249 potential such configuration could be the exposure of highly weatherable nonradiogenic rocks of the Deccan  
250 volcanic series of India and the Ethiopian Traps, located just north of the equator in the late Oligocene (Kent and  
251 Muttoni, 2013).

252 It has also been proposed that glaciation can affect the weatherability of bedrock. Generally, highest riverine  
253 dissolved Sr fluxes are produced from reactive young volcanic rock, as well as soluble carbonates, but the  
254 mechanical flouring of less reactive rock types by glacial erosion can significantly increase their weatherability  
255 and Sr contribution to the ocean. It has been suggested that weathering intensity of the Antarctic craton may have  
256 evolved over the late Eocene through Oligocene, as glacial flouring of Antarctic bedrock increased the  
257 weatherability of this continental Sr source (Miller et al., 1991; Oslick et al., 1994), contributing to the rise in  
258 ocean  $^{87}\text{Sr}/^{86}\text{Sr}$ . Intermittent glaciation, characterized by significant changes in the spatial extent of ice coverage,  
259 may alternately generate highly weatherable fine grained silicates in a subglacial weathering-limited environment  
260 (low continental Sr fluxes) and then expose them to subaerial conditions of enhanced chemical weathering (high  
261 continental Sr flux). On previous biostratigraphic age models, apparent accelerations in the rate of  $^{87}\text{Sr}/^{86}\text{Sr}$   
262 increase at 32, 28, 22.4, 19.5, and 16.5 Ma (on the Cande and Kent timescale) occur 1 m.y after deglaciation  
263 midpoint inferred from benthic  $\delta^{18}\text{O}$  maxima in ODP 747 (Oslick et al., 1994). This was interpreted to result from  
264 the deglacial exposure which may have contributed to a transient increase in flux of radiogenic Sr to the ocean.  
265 With higher resolution benthic  $\delta^{18}\text{O}$  from 1218, we resolve more rapid responses of the  $^{87}\text{Sr}/^{86}\text{Sr}$  ratio to several  
266 deglaciation phases.

267 East Antarctica is inferred to be underlain dominantly by Proterozoic and Archean bedrock (Kirkham et  
268 al., 1995). Exposed bedrock in East Antarctica is dominated by Archean and Proterozoic metamorphic rocks,  
269 with Paleozoic igneous and sedimentary rocks additionally exposed in the Transantarctic mountains (Licht and  
270 Hemming, 2017). Although the Sr isotopic composition of bedrock in Antarctica can be measured directly only  
271 in current exposures in the Transantarctic mountains and coastal areas, crustal rocks at the perimeters of major ice  
272 sheets may represent a major source of the sediment arriving at the margin and therefore weatherable during  
273 retreat (Farmer et al., 2003). Because erosion rates are highest at the perimeter of Antarctic ice sheet (Jamieson  
274 et al., 2010), the mapped bedrock in coastal areas may provide a reasonable representation of the source of  
275 sediment arriving to the glacial margin and weatherable during retreat. Additionally, the fine grained component  
276 of LGM tills exposed in the Ross Sea embayment provide constraints on modern underlying composition of  
277 present erosion (Farmer et al., 2006). Present till composition includes very radiogenic compositions up to 0.740  
278 attributed to erosion of the Neoproterozoic Beardsmore Formation, and compositions in the range of 0.720 to  
279 0.735 typical of 500 Ma Granite Harbor Intursive rocks exposed in southern part of Transantarctic Mountains and  
280 the Wilson terrane Proterozoic gneisses (Farmer et al., 2006). However, a caveat is that the currently exposed  
281 bedrock may be older than that exposed in the Oligocene due to denudation, and younger, less radiogenic bedrocks  
282 may have contributed more to glacial flouring in the Oligocene, making global fluxes less sensitive to the Antarctic  
283 weathering regime.

## 284 4.2 Sr isotope constraints on age models of Site U1406 and Site 1168

285 Previous approaches for Sr isotope stratigraphy for the Cenozoic have inferred a continuous rise in  
286  $^{87}\text{Sr}/^{86}\text{Sr}$ . The data from Site 1218 suggest several intervals with a negligible rate of rise and/or reversals. In the  
287 interval from 28 to 30 Ma, 5 of our 9 samples feature  $^{87}\text{Sr}/^{86}\text{Sr}$  ratios whose analytical 95% CI fall outside of the  
288 bounds of the reference  $^{87}\text{Sr}/^{86}\text{Sr}$  curve of that age generated from biostratigraphically constrained age models  
289 (Mcarthur et al., 2020). For these intervals, particularly during the MOGI, age assignments from Sr isotope  
290 stratigraphy have a higher uncertainty than previously inferred. In the interval from 28 to 30 Ma, the deviation  
291 between the CENOGRID age and the reference curve ranges from 1.1 Ma older than the reference curve to 0.7  
292 Ma younger, a significantly wider uncertainty than the +/- 120 to 180 ky uncertainty predicted for the reference  
293 curve. In the early Miocene, between 21.7 and 19.4 Ma, a number of our Site 1218 CENOGRID ages also deviate  
294 from the ages from the reference curve, by 0.18 to 0.42 Ma younger, a greater uncertainty than the +/- 70 to 50 ky  
295 reported for the reference curve. Consequently, in deriving ages for Site U1406 and Site 1168 on the CENOGRID  
296 scale from  $^{87}\text{Sr}/^{86}\text{Sr}$ , we expand the bounds of the age uncertainties from (Mcarthur et al., 2020) to encompass  
297 the Site 1218 data (Figure 2, green bounds). The width of the resulting age uncertainty therefore ranges from 300  
298 ky in the early Miocene to 1.6 My in the early-mid Oligocene.

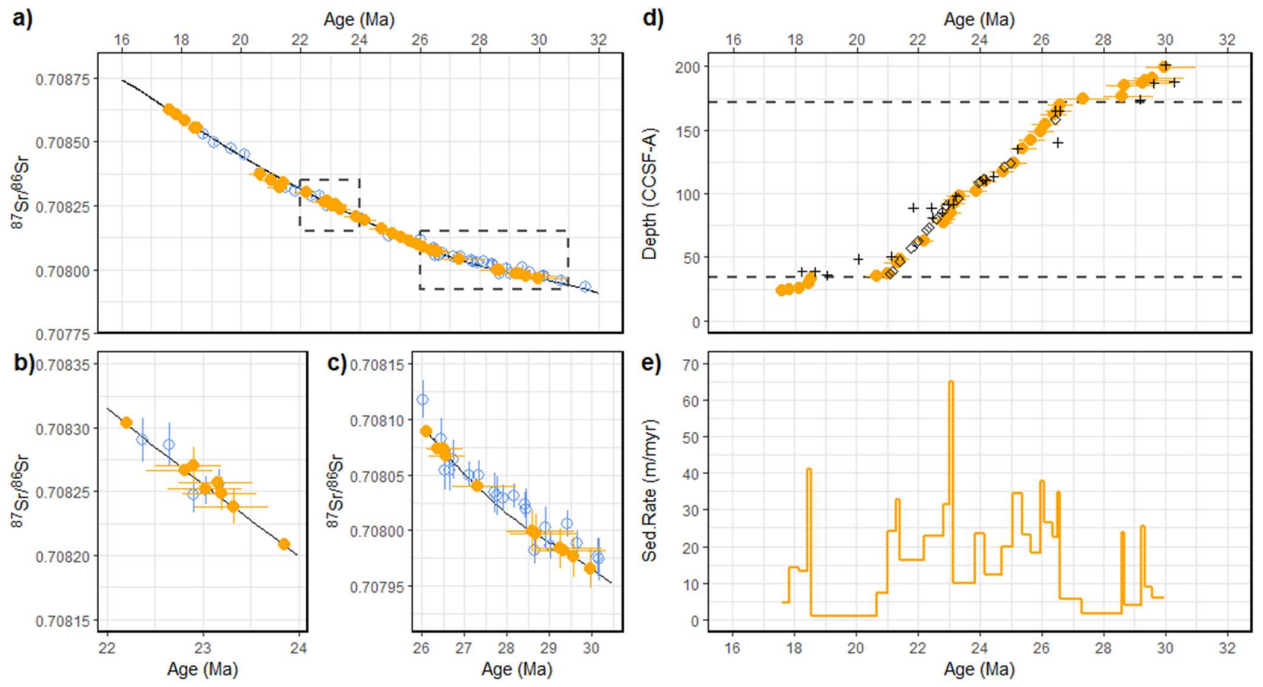
299 In addition to these greater uncertainties, stratigraphic constraints prohibit reversals in ages where there  
300 is no independent evidence for reworking or sediment disturbance. Our Site 1218 data indicate that reversals in  
301  $^{87}\text{Sr}/^{86}\text{Sr}$  are certain within the time interval of 29-26 Ma, and likely at the OMT. Thus, in estimating ages for  
302 1168 and U1406 based on  $^{87}\text{Sr}/^{86}\text{Sr}$ , we assign an initial age based on (McArthur et al 2020) but adjust the age to  
303 preserve stratigraphic relationships (eg no age reversals in our age assignments). The detailed age models are  
304 shown in Tables 2 and Table 3.

### 305 4.2.1. Site U1406

306 A condensed interval and hiatus have been recognized in the Oligocene to early Miocene sediments of  
307 U1406 on the basis of bio- and magnetostratigraphy (Figure 5 ) (Norris et al., 2014; van Peer et al., 2017a).  
308 Because of the slow rate of the Site U1406  $^{87}\text{Sr}/^{86}\text{Sr}$  change and reversals during the MOGI, the U1406  $^{87}\text{Sr}/^{86}\text{Sr}$   
309 cannot precisely pinpoint the duration of the hiatus or condensed interval between 153 and 149 m (CSF-A) (Figure  
310 5). The condensed interval could contain 2 m.y. (28.45 to 26.58 Ma) or < 1 m.y. (27.3 to 26.58). On the other  
311 hand, the early Miocene condensed interval between 27 and 25 m (CSF-A) is constrained to represent 2 m.y.  
312 Sustained high sedimentation rates are confirmed between 21 and 26 Ma. Between 26.4 and 21 Ma, the  $^{87}\text{Sr}/^{86}\text{Sr}$   
313 age model is in close agreement with that devised from magnetostratigraphy (Van Peer et al., 2017a). The Site  
314 1406  $^{87}\text{Sr}/^{86}\text{Sr}$  data indicate that the uppermost 25 m of sediment in U1406, difficult to date due to sparse  
315 biostratigraphic markers, was likely deposited between 18.5 and 17.6 Ma.

316

317



318  
 319  
 320

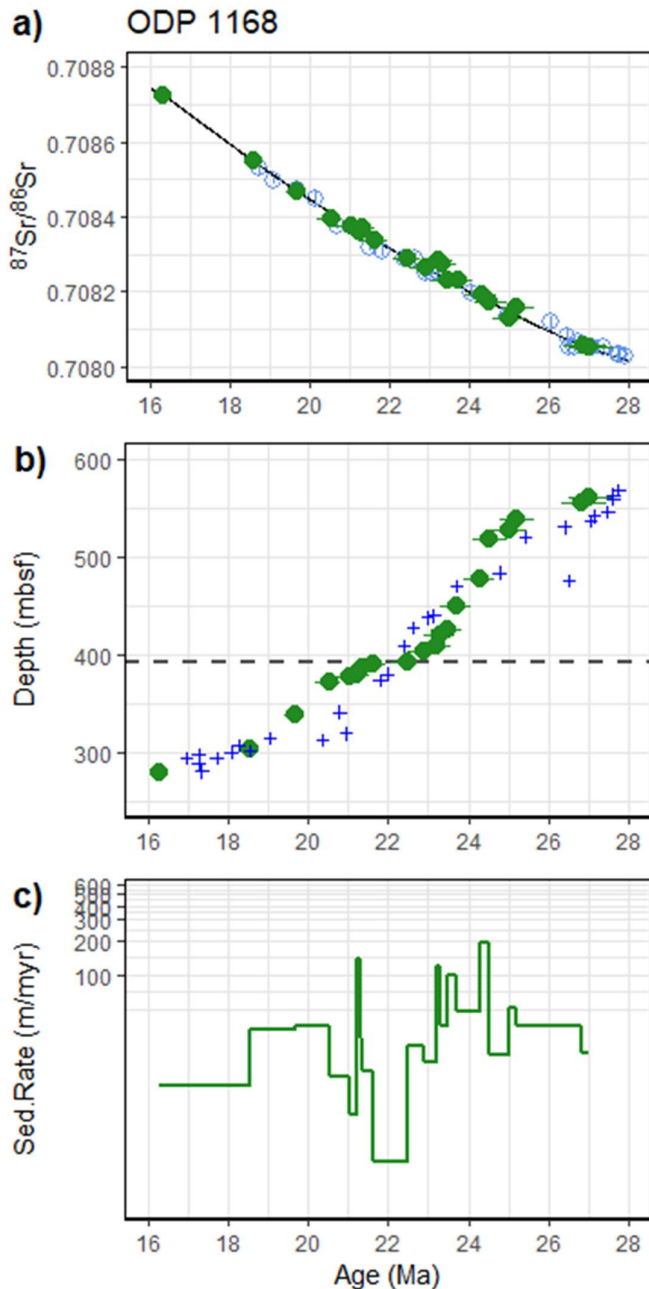


Figure 5. a) Site U1406  $^{87}\text{Sr}/^{86}\text{Sr}$  data (orange) vs age (CENOGRID scale) assigned here; also shown are the Site 1218 new data (blue) and the GTS LOESS curve (Mearthur et al., 2020). b. and c. show insets. For Site U1406, horizontal lines indicate the uncertainty in the age assignments. d) Age depth plot for U1406A on the CSF-A scale. Orange circles denote the ages from  $^{87}\text{Sr}/^{86}\text{Sr}$  compared to previous biostratigraphy tiepoints (crosses; (Norris et al., 2014)) and magnetostratigraphy (open diamonds) (van Peer et al., 2017a). Horizontal dashed lines delimit the strongly condensed intervals; e) the inferred sedimentation rate.

#### 4.2.2. Site 1168

This first  $^{87}\text{Sr}/^{86}\text{Sr}$  stratigraphy for Site 1168 implies significant differences in inferred ages compared to existing biostratigraphy, including significantly higher sedimentation rates in the early Miocene (20.5 to 18.5 Ma), but comparably slower sedimentation rates between 21.6 and 22.5 Ma just after the OMT (Figure 6). This is slightly earlier than the early Miocene hiatus found in many deep sea sedimentary records between 19 to 20 Ma; however, in other deep sea records the precise timing of early Miocene depositional gaps is not yet resolved and could coincide with the condensed interval in 1168 (Sibert and Rubin, 2021). Age assignments remain less precise in the middle Oligocene (25 to 27 Ma) due to the low rate of change and reversals in  $^{87}\text{Sr}/^{86}\text{Sr}$  during this time interval, as well as the

356

357 current low  $^{87}\text{Sr}/^{86}\text{Sr}$  sample coverage.

358

359 Figure 6: a) Site 1168  $^{87}\text{Sr}/^{86}\text{Sr}$  data (green) vs age (CENOGRID scale) assigned here; also shown are the Site 1218 new  
 360 data (blue open symbols) and the GTS LOESS curve (Mearthur et al., 2020) b). Age depth plot for Site 1168. Green  
 361 diamonds denote the ages from  $^{87}\text{Sr}/^{86}\text{Sr}$  compared to previous biostratigraphy derived tie points (crosses). c)  
 362 Sedimentation rate implied by the  $^{87}\text{Sr}/^{86}\text{Sr}$  age model. The horizontal dashed line in b) highlights the period of  
 363 significantly slowed sedimentation of the Early Miocene.

364 **5 Conclusions**

365 The  $^{87}\text{Sr}/^{86}\text{Sr}$  record from the astrochronologically dated Site 1218 provides the opportunity to assess ~1 m.y.  
366 variations in the Sr flux to the ocean during a period of dynamic Antarctic cryosphere evolution. Our dataset  
367 resolves relationships between the locus and/or intensity of continental weathering and phases of Antarctic  
368 glaciation. Overall, the data suggest that the major changes in mid-Oligocene high latitude climate –particularly  
369 the onset and end of the MOGI – do exhibit a close coupling between seawater  $^{87}\text{Sr}/^{86}\text{Sr}$  and benthic  $\delta^{18}\text{O}$ . During  
370 periods of expanded ice coverage on Antarctica such as the MOGI, then, our data are consistent with either  
371 northward shifts in the ITCZ precipitation to areas of nonradiogenic bedrock, and/or lowered weathering fluxes  
372 from highly radiogenic glacial flours on Antarctic. Future, higher resolution sampling is required to further  
373 evaluate the significance of such changes. Additionally, the new  $^{87}\text{Sr}/^{86}\text{Sr}$  record from sites 1168 and U1406  
374 improve the precision of age correlation of these Northern Hemisphere and Southern Hemisphere mid-latitude  
375 sites with each other and with high resolution benthic  $\delta^{18}\text{O}$  records aligned to the CENOGRID chronology.

376 **Competing interests**

377 The contact author has declared that none of the authors has any competing interests.

378 **Acknowledgments**

379 This study was supported by the Swiss National Science Foundation (Award 200021\_182070 to Heather M. Stoll).  
380 We thank Romain Alosius for assistance picking foraminifera, and Laura Arnold for initial evaluation of  
381 foraminifera preservation. We gratefully acknowledge the Ocean Drilling Program and International Ocean  
382 Discovery Program for providing the samples used in this study.

383 **Author contributions**

384 The study was conceived by HMS. Samples were selected by HMS with advice from HP. Foraminifera were  
385 prepared by JG, IHA, and TT. Sr isotope analyses were completed by LDP. Interpretation was completed by  
386 HMS and figures were prepared by HMS and JG. The manuscript was written by HMS with input from all  
387 authors.

388

389

390

391 Table 1. ODP identifiers, CENOGRID age, and  $^{87}\text{Sr}/^{86}\text{Sr}$  data for Site 1218.

Lab ID	Exp	Site	Hole	Core	Core Type	Section	Section Half	Top Interval (cm)	Bottom Interval (cm)	depth (mcd, m)	$^{86}\text{Sr}$ CENOGRID (Ma)	$^{87}\text{Sr}/^{86}\text{Sr}$	Internal SE (2 $\sigma$ )
B2	199	1218	B	7	H	1	W	125	130	59.93	18.73	0.708529	1.71E-05
B3	199	1218	B	7	H	3	W	75	80	62.43	19.10	0.708497	1.13E-05
A1	199	1218	A	7	H	3	W	50	55	67.29	19.67	0.708473	1.21E-05
A2	199	1218	A	7	H	5	W	50	55	70.29	20.12	0.708448	1.71E-05
B4	199	1218	B	8	H	3	W	100	105	73.29	20.66	0.708378	1.17E-05
B5	199	1218	B	9	H	3	W	32	37	82.07	21.50	0.708320	1.21E-05
B6	199	1218	B	9	H	5	W	105	110	85.45	21.82	0.708309	1.71E-05
A4	199	1218	A	9	H	4	W	82	87	90.32	22.37	0.708290	1.71E-05
A5	199	1218	A	9	H	6	W	20	25	92.67	22.65	0.708287	1.71E-05
B7	199	1218	B	10	H	3	W	82	87	94.54	22.90	0.708248	1.50E-05
B8	199	1218	B	10	H	4	W	87	92	96.12	23.03	0.708251	1.06E-05
B9	199	1218	B	10	H	5	W	141	146	98.17	23.17	0.708256	1.19E-05
B11	199	1218	B	11	H	3	W	147	150	107.26	24.06	0.708199	1.71E-05
B12	199	1218	B	12	H	3	W	107	112	118.18	24.95	0.708133	1.71E-05
B13	199	1218	B	13	H	6	W	17	22	131.57	26.03	0.708118	1.71E-05
1218A 14H1 15-25cm	199	1218	A	14	H	1	W	15	25	138.00	26.46	0.708083	1.82E-05
A9	199	1218	A	14	H	1	W	100	105	138.73	26.52	0.708054	1.71E-05
1218A 14H2 115cm	199	1219	A	15	H	2	W	115	117	140.27	26.64	0.708054	1.84E-05
A10	199	1218	A	14	H	3	W	80	85	141.59	26.74	0.708064	1.71E-05
1218B 15H1 35cm	199	1218	B	15	H	1	W	35	38		27.04	0.708070	1.86E-05
B14	199	1218	B	15	H	2	W	30	35	147.04	27.10	0.708050	1.13E-05
B15	199	1218	B	15	H	4	W	80	85	150.56	27.34	0.708050	1.33E-05
1218B 16H1 25cm	199	1218	B	16	H	1	W	25	26.5	156.17	27.71	0.708034	1.82E-05
B16	199	1218	B	16	H	1	W	70	75	156.63	27.75	0.708031	1.71E-05
B17	199	1218	B	16	H	2	W	107	112	158.55	27.91	0.708029	1.21E-05
B18	199	1218	B	16	H	5	W	60	65	162.03	28.15	0.708031	1.13E-05
C1	199	1218	C	10	H	2	W	100	105	164.77	28.42	0.708023	1.13E-05
1218C 10H3 5cm	199	1218	C	10	H	3	W	5	7	165.25	28.45	0.708019	1.82E-05
B19	199	1218	B	17	H	3	W	120	125	170.40	28.65	0.707982	1.21E-05
1218C 11H1 115cm	199	1218	C	11	H	1	W	115	117	173.77	28.91	0.708003	1.84E-05
C2	199	1218	C	11	H	2	W	130	135	175.45	29.03	0.707986	1.21E-05
B20	199	1218	B	18	H	5	W	10	15	182.15	29.43	0.708006	1.21E-05
A11	199	1218	A	18	H	4	W	37	45	185.68	29.66	0.707988	1.12E-05
A12	199	1218	A	19	H	2	W	67	75	192.20	30.14	0.707976	1.71E-05
1218C 12H6 85cm	199	1218	C	12	X	6	W	85	87	191.63	30.17	0.707974	1.91E-05
B21	199	1218	B	20	X	3	W	117	122	199.97	30.73	0.707956	1.71E-05
B23	199	1218	B	21	X	4	W	12	17	211.94	31.55	0.707930	1.50E-05

392

393

394

395

396

397

398

Table 2.  $^{87}\text{Sr}/^{86}\text{Sr}$  data for Site U1406 and the assigned ages and age uncertainties.

Site	Hole	Core	Core Type	Section	Section Half	Top Interval (cm)	Bottom Interval (cm)	Depth CSF-A (m)	Depth CCSF-A (m)	$^{87}\text{Sr}/^{86}\text{Sr}$	Internal SE (2 $\sigma$ )	midpoint age assigned (Ma)	lower age (Ma)	upper age (Ma)
1406	A	2	H	4	w	89	93	11.61	23.9	0.708625	0.000018	17.60	17.45	17.75
1406	A	2	H	5	w	36	40	12.58	24.9	0.708607	0.000018	17.82	17.67	17.97
1406	A	3	H	2	w	5	8	17.14	25.7	0.708582	0.000004	18.14	17.99	18.29
1406	A	3	H	4	w	89	92	20.98	29.6	0.708556	0.000004	18.43	18.28	18.58
1406	A	3	H	7	w	8	12	24.68	33.3	0.708556	0.000004	18.52	18.30	18.70
1406	A	4	h	1	w	139	143	26.61	34.7	0.708372	0.000004	20.66	20.29	20.91
1406	A	4	H	3	w	81	85	29.03	37.2	0.708350	0.000004	21.00	20.60	21.30
1406	A	5	H	2	w	6	9	36.27	45.4	0.708323	0.000003	21.30	20.90	21.60
1406	A	5	H	4	w	33	37	39.55	48.7	0.708341	0.000004	21.40	21.00	21.70
1406	A	6	H	6	w	74	80	52.47	63.0	0.708303	0.000004	22.20	21.80	22.50
1406	A	8	H	3	w	16	22	66.39	77.6	0.708267	0.000003	22.81	22.41	23.11
1406	C	8	H	1	w	80	84		80.3	0.708271	0.000014	22.90	22.50	23.20
1406	A	9	H	1	w	62	68	73.35	84.8	0.708252	0.000005	23.03	22.63	23.41
1406	A	9	H	6	w	91	95	81.16	92.6	0.708257	0.000004	23.15	22.75	23.53
1406	B	10	H	3	w	140	144		95.6	0.708249	0.000013	23.19	22.79	23.57
1406	B	10	H	5	w	70	74		97.9	0.708238	0.000013	23.32	22.92	23.69
1406	A	10	H	4	w	127	133	88.00	101.8	0.708208	0.000004	23.85	23.45	24.23
1406	A	11	H	3	w	53	59	95.26	109.2	0.708191	0.000004	24.16	23.76	24.54
1406	A	12	H	1	w	90	94	102.12	117.3	0.708161	0.000006	24.72	24.32	25.09
1406	A	12	H	6	w	44	48	109.16	124.4	0.708142	0.000007	25.07	24.67	25.52
1406	A	13	H	7	w	21	25	119.45	135.0	0.708126	0.000004	25.37	24.97	25.82
1406	A	14	H	4	w	97	103	125.70	141.8	0.708112	0.000007	25.64	25.24	26.09
1406	A	15	H	2	w	6	10	131.28	148.7	0.708097	0.000003	25.95	25.55	26.40
1406	A	15	H	5	w	103	107	136.81	154.3	0.708090	0.000004	26.10	25.70	26.55
1406	A	16	H	4	w	26	30	143.98	162.1	0.708074	0.000004	26.37	25.97	26.82
1406	A	16	H	6	w	66	70	147.38	165.5	0.708074	0.000005	26.52	26.12	26.97
1406	A	17	H	1	w	128	132	149.40	170.1	0.708068	0.000005	26.58	26.18	27.03
1406	A	17	H	4	w	86	90	153.48	174.2	0.708039	0.000003	27.31	26.71	28.21
1406	A	17	H	5	w	136	140	155.48	176.2	0.707999	0.000018	28.59	27.99	29.59
1406	A	18	H	1	w	19	23	157.51	184.7	0.707997	0.000018	28.68	28.08	29.68
1406	A	18	H	2	w	94	98	159.60	186.8	0.707984	0.000018	29.24	28.64	30.24
1406	A	18	H	4	w	20	24	161.86	189	0.707982	0.000004	29.33	28.73	30.33
1406	A	18	H	5	w	96	100	164.12	191	0.707976	0.000018	29.58	28.98	30.58
1406	A	19	H	2	w	15	19	166.37	200	0.707966	0.000018	29.97	29.37	30.97

399

400

401

402

403

404

Table 3. <sup>87</sup>Sr/<sup>86</sup>Sr data for Site 1168 and the assigned ages and age uncertainties.

Site	Hole	Core	Core Type	Section	Section Half	Top Interval (cm)	Bottom Interval (cm)	Depth (mbsf)	<sup>87</sup> Sr/ <sup>86</sup> Sr	Internal SE (2σ)	central age (Ma)	min age (Ma)	max age (Ma)
1168	A	30	X	5	W	2	8	278.25	0.708724	1.82E-05	<b>16.29</b>	16.14	16.44
1168	A	33	X	2	W	52	58	302.75	0.7085492	1.82E-05	<b>18.57</b>	18.35	18.74
1168	A	37	X	1	W	43	49	339.26	0.7084685	1.82E-05	<b>19.67</b>	19.39	19.87
1168	A	40	X	3	W	59.5	64.5	371.22	0.7083942	1.82E-05	<b>20.55</b>	20.18	20.80
1168	A	41	X	1	W	5	7.5	377.36	0.7083771	1.41E-05	<b>21.02</b>	20.62	21.32
1168	A	41	X	1	W	135	138	378.66	0.7083633	1.35E-05	<b>21.24</b>	20.84	21.54
1168	A	41	X	6	W	34	36.5	385.15	0.7083596	1.35E-05	<b>21.28</b>	20.88	21.58
1168	A	41	X	7	W	34	47.5	386.46	0.7083715	1.41E-05	<b>21.33</b>	20.93	21.63
1168	A	42	X	3	W	45	25.5	390.78	0.7083377	1.62E-05	<b>21.63</b>	21.23	21.93
1168	A	42	X	4	W	137	139	392.78	0.7082875	1.76E-05	<b>22.47</b>	22.07	22.77
1168	A	43	X	5	W	55	57	403.06	0.7082624	1.95E-05	<b>22.90</b>	22.50	23.28
1168	A	44	X	2	W	69	71	408.3	0.7082843	1.95E-05	<b>23.20</b>	22.80	23.58
1168	A	45	X	3	W	143	145	420.14	0.708272	1.92E-05	<b>23.30</b>	22.90	23.68
1168	A	46	X	1	W	49	55	425.82	0.7082296	1.82E-05	<b>23.46</b>	23.06	23.84
1168	A	48	X	4	W	65	67.5	449.65	0.708231	1.95E-05	<b>23.70</b>	23.30	24.08
1168	A	51	X	4	W	38	42	478.2	0.7081923	1.82E-05	<b>24.30</b>	23.90	24.68
1168	A	55	X	5	W	33	39	518.06	0.7081716	1.82E-05	<b>24.51</b>	24.11	24.96
1168	A	56	X	5	W	37	43	527.8	0.7081292	1.82E-05	<b>25.00</b>	24.60	25.45
1168	A	57	X	5	W	113	117	538.25	0.7081581	1.86E-05	<b>25.20</b>	24.80	25.65
1168	A	59	X	4	W	83	87	555.75	0.7080568	2.19E-05	<b>26.84</b>	26.34	27.44
1168	A	60	X	2	W	57	61	562.09	0.7080503	1.84E-05	<b>27.02</b>	26.52	27.62

405

406

407

408

409

410

411



412 **References**

413

414

415

- 416 Atwood, A. R., Donohoe, A., Battisti, D. S., Liu, X., and Pausata, F. S.: Robust longitudinally variable responses of the ITCZ  
 417 to a myriad of climate forcings, *Geophysical Research Letters*, 47, e2020GL088833, doi.org/10.1029/2020GL088833, 2020.  
 418 Boyle, P. R., Romans, B. W., Tucholke, B. E., Norris, R. D., Swift, S. A., and Sexton, P. F.: Cenozoic North Atlantic deep  
 419 circulation history recorded in contourite drifts, offshore Newfoundland, Canada, *Marine Geology*, 385, 185-203,  
 420 doi.org/10.1016/j.margeo.2016.12.014, 2017.  
 421 Cande, S. C. and Kent, D. V.: A new geomagnetic polarity time scale for the Late Cretaceous and Cenozoic, *Journal of*  
 422 *Geophysical Research: Solid Earth*, 97, 13917-13951, doi.org/10.1029/92JB01202, 1992.  
 423 De Vleeschouwer, D., Vahlenkamp, M., Crucifix, M., and Pälike, H.: Alternating Southern and Northern Hemisphere climate  
 424 response to astronomical forcing during the past 35 my, *Geology*, 45, 375-378, doi.org/10.1130/G38663.1, 2017.  
 425 Egger, L. M., Bahr, A., Friedrich, O., Wilson, P. A., Norris, R. D., van Peer, T. E., Lippert, P. C., Liebrand, D., and Pross, J.:  
 426 Sea-level and surface-water change in the western North Atlantic across the Oligocene–Miocene Transition: a palynological  
 427 perspective from IODP Site U1406 (Newfoundland margin), *Marine Micropaleontology*, 139, 57-71,  
 428 doi.org/10.1016/j.marmicro.2017.11.003, 2018.  
 429 Exon, N. F., Kennett, J. P., and Malone, M. J.: Leg 189 synthesis: Cretaceous–Holocene history of the Tasmanian gateway,  
 430 *Proceedings of the ocean drilling program, scientific results*, 1-37, doi:10.2973/odp.proc.sr.189.101.2004,  
 431 Farmer, G. L., Barber, D., and Andrews, J.: Provenance of Late Quaternary ice-proximal sediments in the North Atlantic: Nd,  
 432 Sr and Pb isotopic evidence, *Earth and Planetary Science Letters*, 209, 227-243, doi.org/10.1016/S0012-821X(03)00068-2,  
 433 2003.  
 434 Farmer, G. L., Licht, K., Swope, R. J., and Andrews, J.: Isotopic constraints on the provenance of fine-grained sediment in  
 435 LGM tills from the Ross Embayment, Antarctica, *Earth and Planetary Science Letters*, 249, 90-107,  
 436 doi.org/10.1016/j.epsl.2006.06.044, 2006.  
 437 Galy, A., France-Lanord, C., and Derry, L. A.: The Late Oligocene–Early Miocene Himalayan belt constraints deduced from  
 438 isotopic compositions of Early Miocene turbidites in the Bengal Fan, *Tectonophysics*, 260, 109-118, 1996.  
 439 Guitián, J. and Stoll, H. M.: Evolution of Sea Surface Temperature in the Southern Mid-latitudes from Late Oligocene through  
 440 Early Miocene, *Paleoceanography and Paleoclimatology*, 36, e2020PA004199, doi.org/10.1029/2020PA004199, 2021.  
 441 Hodell, D. A., Mead, G. A., and Mueller, P. A.: Variation in the strontium isotopic composition of seawater (8 Ma to present):  
 442 Implications for chemical weathering rates and dissolved fluxes to the oceans, *Chemical Geology: Isotope Geoscience section*,  
 443 80, 291-307, 1990.  
 444 Hoem, F. S., Sauermilch, I., Hou, S., Brinkhuis, H., Sangiorgi, F., and Bijl, P. K.: Late Eocene–early Miocene evolution of the  
 445 southern Australian subtropical front: a marine palynological approach, *Journal of*  
 446 *Micropalaeontology*, 40, 175-193, doi.org/10.5194/jm-40-175-2021, 2021, 2021.  
 447 Hoem, F. S., Sauermilch, I., Aleksinski, A. K., Huber, M., Peterse, F., Sangiorgi, F., and Bijl, P. K.: Strength and variability  
 448 of the Oligocene Southern Ocean surface temperature gradient, *Communications Earth & Environment*, 3, 322,  
 449 doi.org/10.1038/s43247-022-00666-5, 2022.  
 450 Holbourn, A., Kuhnt, W., Kochhann, K. G., Andersen, N., and Sebastian Meier, K.: Global perturbation of the carbon cycle  
 451 at the onset of the Miocene Climatic Optimum, *Geology*, 43, 123-126, doi.org/10.1130/G36317.1, 2015.  
 452 Jamieson, S. S., Sugden, D. E., and Hulton, N. R.: The evolution of the subglacial landscape of Antarctica, *Earth and Planetary*  
 453 *Science Letters*, 293, 1-27, doi.org/10.1016/j.epsl.2010.02.012, 2010.  
 454 Kent, D. V. and Muttoni, G.: Modulation of Late Cretaceous and Cenozoic climate by variable drawdown of atmospheric pCO  
 455 2 from weathering of basaltic provinces on continents drifting through the equatorial humid belt, *Climate of the Past*, 9, 525-  
 456 546, doi.org/10.5194/cp-9-525-2013, 2013.  
 457 Kim, B. and Zhang, Y. G.: Methane hydrate dissociation across the Oligocene–Miocene boundary, *Nature Geoscience*, 15,  
 458 203-209, doi.org/10.1038/s41561-022-00895-5, 2022.  
 459 Kirkham, R., Chorlton, L., and Carriere, J.: Generalized geology of the world, Generalized geological map of the world and  
 460 linked databases. Geological Survey of Canada, Open File 2915d, 1995.  
 461 Krishnaswami, S., Trivedi, J., Sarin, M., Ramesh, R., and Sharma, K.: Strontium isotopes and rubidium in the Ganga-  
 462 Brahmaputra river system: Weathering in the Himalaya, fluxes to the Bay of Bengal and contributions to the evolution of  
 463 oceanic 87Sr/86Sr, *Earth and Planetary Science Letters*, 109, 243-253, doi.org/10.1016/0012-821X(92)90087-C, 1992.  
 464 Licht, K. J. and Hemming, S. R.: Analysis of Antarctic glacial sediment provenance through geochemical and petrologic  
 465 applications, *Quaternary Science Reviews*, 164, 1-24, doi.org/10.1016/j.quascirev.2017.03.009, 2017.  
 466 Liebrand, D., Beddow, H. M., Lourens, L. J., Pälike, H., Raffi, I., Bohaty, S. M., Hilgen, F. J., Saes, M. J., Wilson, P. A., and  
 467 van Dijk, A. E.: Cyclostratigraphy and eccentricity tuning of the early Oligocene through early Miocene (30.1–17.1 Ma):  
 468 *Cibicides mundulus* stable oxygen and carbon isotope records from Walvis Ridge Site 1264, *Earth and Planetary Science*  
 469 *Letters*, 450, 392-405, doi.org/10.1016/j.epsl.2016.06.007, 2016.  
 470 Liebrand, D., de Bakker, A. T., Beddow, H. M., Wilson, P. A., Bohaty, S. M., Ruessink, G., Pälike, H., Batenburg, S. J.,  
 471 Hilgen, F. J., and Hodell, D. A.: Evolution of the early Antarctic ice ages, *Proceedings of the National Academy of Sciences*,  
 472 114, 3867-3872, 2017.  
 473 Liu, Z., He, Y., Jiang, Y., Wang, H., Liu, W., Bohaty, S. M., and Wilson, P. A.: Transient temperature asymmetry between  
 474 hemispheres in the Palaeogene Atlantic Ocean, *Nature Geoscience*, 11, 656-660, doi.org/10.1038/s41561-018-0182-9, 2018.

475 McArthur, J., Howarth, R., Shields, G., and Zhou, Y.: Strontium isotope stratigraphy, in: *Geologic time scale 2020*, Elsevier,  
476 211-238, doi.org/10.1016/B978-0-12-824360-2.00007-3, 2020.

477 Mead, G. A. and Hodell, D. A.: Controls on the  $87\text{Sr}/86\text{Sr}$  composition of seawater from the middle Eocene to Oligocene:  
478 Hole 689B, Maud Rise, Antarctica, *Paleoceanography*, 10, 327-346, doi.org/10.1029/94PA03069, 1995.

479 Miller, K. G., Feigenson, M. D., Kent, D. V., and Olsson, R. K.: Upper Eocene to Oligocene isotope ( $87\text{Sr}/86\text{Sr}$ ,  $\delta^{18}\text{O}$ ,  $\delta^{13}\text{C}$ )  
480 standard section, Deep sea drilling Project site 522, *Paleoceanography*, 3, 223-233, doi.org/10.1029/PA003i002p00223, 1988.

481 Miller, K. G., Feigenson, M. D., Wright, J. D., and Clement, B. M.: Miocene isotope reference section, Deep Sea Drilling  
482 Project Site 608: an evaluation of isotope and biostratigraphic resolution, *Paleoceanography*, 6, 33-52,  
483 doi.org/10.1029/90PA01941, 1991.

484 Myrow, P. M., Hughes, N. C., Derry, L. A., McKenzie, N. R., Jiang, G., Webb, A. A. G., Banerjee, D. M., Paulsen, T. S., and  
485 Singh, B. P.: Neogene marine isotopic evolution and the erosion of Lesser Himalayan strata: Implications for Cenozoic tectonic  
486 history, *Earth and Planetary Science Letters*, 417, 142-150, 2015.

487 Norris, R., Wilson, P., and Blum, P.: Proceedings of the Integrated Ocean Drilling Program Exp. 342, College Station, TX:  
488 Integrated Ocean Drilling Program, doi.org/10.2204/iodp.proc.342.107.2014, 2014.

489 Oslick, J. S., Miller, K. G., Feigenson, M. D., and Wright, J. D.: Oligocene-Miocene strontium isotopes: Stratigraphic revisions  
490 and correlations to an inferred glacioeustatic record, *Paleoceanography*, 9, 427-443, doi.org/10.1029/94PA00249, 1994.

491 Pälike, H., Norris, R. D., Herrle, J. O., Wilson, P. A., Coxall, H. K., Lear, C. H., Shackleton, N. J., Tripathi, A. K., and Wade,  
492 B. S.: The heartbeat of the Oligocene climate system, *science*, 314, 1894-1898, DOI: 10.1126/science.1133822, 2006.

493 Palmer, M. and Elderfield, H.: Sr isotope composition of sea water over the past 75 Myr, *Nature*, 314, 526-528,  
494 doi.org/10.1038/314526a0, 1985.

495 Paytan, A., Griffith, E. M., Eisenhauer, A., Hain, M. P., Wallmann, K., and Ridgwell, A.: A 35-million-year record of seawater  
496 stable Sr isotopes reveals a fluctuating global carbon cycle, *Science*, 371, 1346-1350, 2021.

497 Pena, L., Calvo, E., Cacho, I., Eggins, S., and Pelejero, C.: Identification and removal of Mn-Mg-rich contaminant phases on  
498 foraminiferal tests: Implications for Mg/Ca past temperature reconstructions, *Geochemistry, Geophysics, Geosystems*, 6,  
499 doi.org/10.1029/2005GC000930, 2005.

500 Peucker-Ehrenbrink, B. and Fiske, G. J.: A continental perspective of the seawater  $87\text{Sr}/86\text{Sr}$  record: a review, *Chemical*  
501 *Geology*, 510, 140-165, /doi.org/10.1016/j.chemgeo.2019.01.017, 2019.

502 Raymo, M. E., Ruddiman, W. F., and Froelich, P. N.: Influence of late Cenozoic mountain building on ocean geochemical  
503 cycles, *Geology*, 16, 649-653, doi.org/10.1130/0091-7613(1988)016<0649:IOLCMB>2.3.CO;2, 1988.

504 Reilly, T. J., Miller, K. G., and Feigenson, M. D.: Latest Eocene-earliest Miocene Sr isotopic reference section, Site 522,  
505 eastern South Atlantic, *Paleoceanography*, 17, 18-11-18-19, doi.org/10.1029/2001PA000745, 2002.

506 Scher, H. D., Whittaker, J. M., Williams, S. E., Latimer, J. C., Kordesch, W. E., and Delaney, M. L.: Onset of Antarctic  
507 Circumpolar Current 30 million years ago as Tasmanian Gateway aligned with westerlies, *Nature*, 523, 580-583,  
508 doi.org/10.1038/nature14598, 2015.

509 Sibert, E. C. and Rubin, L. D.: An early Miocene extinction in pelagic sharks, *Science*, 372, 1105-1107, DOI:  
510 10.1126/science.aaz3549, 2021.

511 Spray, J. F., Bohaty, S. M., Davies, A., Bailey, I., Romans, B. W., Cooper, M. J., Milton, J. A., and Wilson, P. A.: North  
512 Atlantic evidence for a unipolar icehouse climate state at the Eocene-Oligocene Transition, *Paleoceanography and*  
513 *Paleoclimatology*, 34, 1124-1138, doi.org/10.1029/2019PA003563, 2019.

514 Stickley, C., Brinkhuis, H., McGonigal, K., Chaproniere, G., Fuller, M., Kelly, D., Nürnberg, D., Pfuhl, H., Schellenberg, S.,  
515 and Schönfeld, J.: Late Cretaceous–Quaternary biomagnetostratigraphy of ODP Sites 1168, 1170, 1171, and 1172, Tasmanian  
516 Gateway, *Proceedings of the Ocean Drilling Program, Scientific Results*, 1-57, doi:10.2973/odp.proc.sr.189.111.2004,  
517 van Peer, T. E., Xuan, C., Lippert, P. C., Liebrand, D., Agnini, C., and Wilson, P. A.: Extracting a detailed magnetostratigraphy  
518 from weakly magnetized, Oligocene to early Miocene sediment drifts recovered at IODP Site U1406 (Newfoundland margin,  
519 northwest Atlantic Ocean), *Geochemistry, Geophysics, Geosystems*, 18, 3910-3928, doi.org/10.1002/2017GC007185, 2017a.

520 van Peer, T. E., Liebrand, D., Xuan, C., Lippert, P. C., Agnini, C., Blum, N., Blum, P., Bohaty, S. M., Bown, P., and Greenop,  
521 R.: Data report: revised composite depth scale and splice for IODP Site U1406, doi:10.2204/iodp.proc.342.202.2017), 2017b.

522 Westerhold, T., Marwan, N., Drury, A. J., Liebrand, D., Agnini, C., Anagnostou, E., Barnett, J. S., Bohaty, S. M., De  
523 Vleeschouwer, D., and Florindo, F.: An astronomically dated record of Earth's climate and its predictability over the last 66  
524 million years, *Science*, 369, 1383-1387, DOI: 10.1126/science.aba685, 2020.

525 Yang, Y., Galy, A., Yang, R., Liu, Y., Zhang, W., Ruan, X., Fang, X., Jin, Z., Song, B., and Yan, M.: Intense metamorphism-  
526 generated radiogenic Sr regulated Cenozoic water Sr isotope evolution on the NE Tibetan Plateau: A perspective on Qilian  
527 orogen denudation and Asian eolian transport, *Geological Society of America Bulletin*, 2022.

528 Zachos, J. C., Opdyke, B. N., Quinn, T. M., Jones, C. E., and Halliday, A. N.: Early Cenozoic glaciation, Antarctic weathering,  
529 and seawater  $87\text{Sr}/86\text{Sr}$ : Is there a link?, *Chemical Geology*, 161, 165-180, doi.org/10.1016/S0009-2541(99)00085-6, 1999.

531